









Study of Time Evolution of Thermal and Nonthermal Emission from an M-class Solar Flare

Shunsaku Nagasawa^{1,2} , Tomoko Kawate^{3,4} , Noriyuki Narukage^{4,5} , Tadayuki Takahashi^{1,2} , Amir Caspi⁶ , and Thomas N. Woods⁷ 

¹ Department of Physics, University of Tokyo, 7-3-1 Hongo, Bunkyo, Tokyo 113-0033, Japan; shunsaku.nagasawa@ipmu.jp

² Kavli Institute for the Physics and Mathematics of the Universe (Kavli IPMU, WPI) The University of Tokyo, 5-1-5 Kashiwanoha, Kashiwa, Chiba 277-8583, Japan

³ National Institute for Fusion Science, 322-6 Oroshi-cho, Toki, Gifu 509-5292 Japan

⁴ The Graduate University for Advanced Studies (SOKENDAI), Shonan-Kokusai Village, Hayama, Miura, Kanagawa 240-0193 Japan

⁵ National Astronomical Observatory of Japan, Mitaka, Tokyo 181-8588, Japan

⁶ Southwest Research Institute, 1050 Walnut St., Suite 300, Boulder, CO 80302, USA

⁷ Laboratory for Atmospheric and Space Physics, University of Colorado at Boulder, 3665 Discovery Dr., Boulder, CO 80303, USA

Received 2022 January 28; revised 2022 May 2; accepted 2022 May 27; published 2022 July 13

Abstract

We conduct a wide-band X-ray spectral analysis in the energy range of 1.5–100 keV to study the time evolution of the M7.6-class flare of 2016 July 23, with the Miniature X-ray Solar Spectrometer (MinXSS) CubeSat and the Reuven Ramaty High Energy Solar Spectroscopic Imager (RHESSI) spacecraft. With the combination of MinXSS for soft X-rays and RHESSI for hard X-rays, a nonthermal component and three-temperature multithermal component—“cool” ($T \approx 3$ MK), “hot” ($T \approx 15$ MK), and “superhot” ($T \approx 30$ MK)—were measured simultaneously. In addition, we successfully obtained the spectral evolution of the multithermal and nonthermal components with a 10 s cadence, which corresponds to the Alfvén timescale in the solar corona. We find that the emission measures of the cool and hot thermal components are drastically increasing more than hundreds of times and the superhot thermal component is gradually appearing after the peak of the nonthermal emission. We also study the microwave spectra obtained by the Nobeyama Radio Polarimeters, and we find that there is continuous gyrosynchrotron emission from mildly relativistic nonthermal electrons. In addition, we conducted a differential emission measure (DEM) analysis by using Atmospheric Imaging Assembly on board the Solar Dynamics Observatory and determined that the DEM of cool plasma increases within the flaring loop. We find that the cool and hot plasma components are associated with chromospheric evaporation. The superhot plasma component could be explained by the thermalization of the nonthermal electrons trapped in the flaring loop.

Unified Astronomy Thesaurus concepts: [Non-thermal radiation sources \(1119\)](#); [Solar flares \(1496\)](#)

Supporting material: animation

1. Introduction

Solar flares are powerful explosions, releasing coronal magnetic energy up to $\sim 10^{33}$ erg on short timescales (100–1000 s) and efficiently accelerating electrons up to several hundreds of MeV and ions to tens of GeV (Holman et al. 2011). It has been established that magnetic reconnection plays an important role during solar flares (Shibata & Magara 2011). Magnetic reconnection is a process in which oppositely oriented components of the magnetic field annihilate, the magnetic field reconfigures to a lower-energy state, and the liberated free energy of the magnetic field in the plasma is efficiently converted into particle kinetic energy through acceleration and plasma heating (see Hesse & Cassak 2020, for a review). However, the total amount of magnetic energy released by magnetic reconnection and the proportion of distributed energy to the nonthermal particles and plasma heating remain poorly understood.

During solar flares, the energy released through magnetic reconnection is converted into other forms through processes such as heating of coronal plasma, bulk flows within coronal mass ejections, and particle acceleration (see Benz 2017, for a

review). In addition, accelerated particles secondarily contribute to plasma heating through their collisions with the ambient plasma. In this way, the heating, cooling, and particle acceleration processes should be closely related to the magnetic reconnection and correlated to each other. Therefore, to resolve such a complicated energy conversion system, it is crucial to separate and follow the time evolution of “thermal emission” from heated plasma and “nonthermal emission” from accelerated electrons (Shibata 1996; Holman et al. 2011) as a first step.

The multithermal structure of flares has been studied in the extreme-ultraviolet (EUV; $E \approx 0.01$ – 0.2 keV) band using emission lines from multiply ionized Fe, e.g., with the EUV Variability Experiment (EVE; Woods et al. 2012) on the Solar Dynamics Observatory (SDO). Warren et al. (2013) analyzed differential emission measure (DEM) distributions using Fe XV–Fe XXIV lines observed by SDO/EVE and showed that the isothermal approximation is not an appropriate representation of the thermal structure. However, EUV observations alone have poor sensitivity to thermal emission from plasmas hotter than ~ 15 – 20 MK (Winebarger et al. 2012), particularly for “superhot” temperatures ($T \gtrsim 30$ MK; e.g., Caspi & Lin 2010), and are also not sensitive to nonthermal emission. Moreover, since the timescale to reach ionization equilibrium for line emission may be longer than the timescales of relevant dynamic processes, spectral analysis using continuum emission



Original content from this work may be used under the terms of the [Creative Commons Attribution 4.0 licence](#). Any further distribution of this work must maintain attribution to the author(s) and the title of the work, journal citation and DOI.

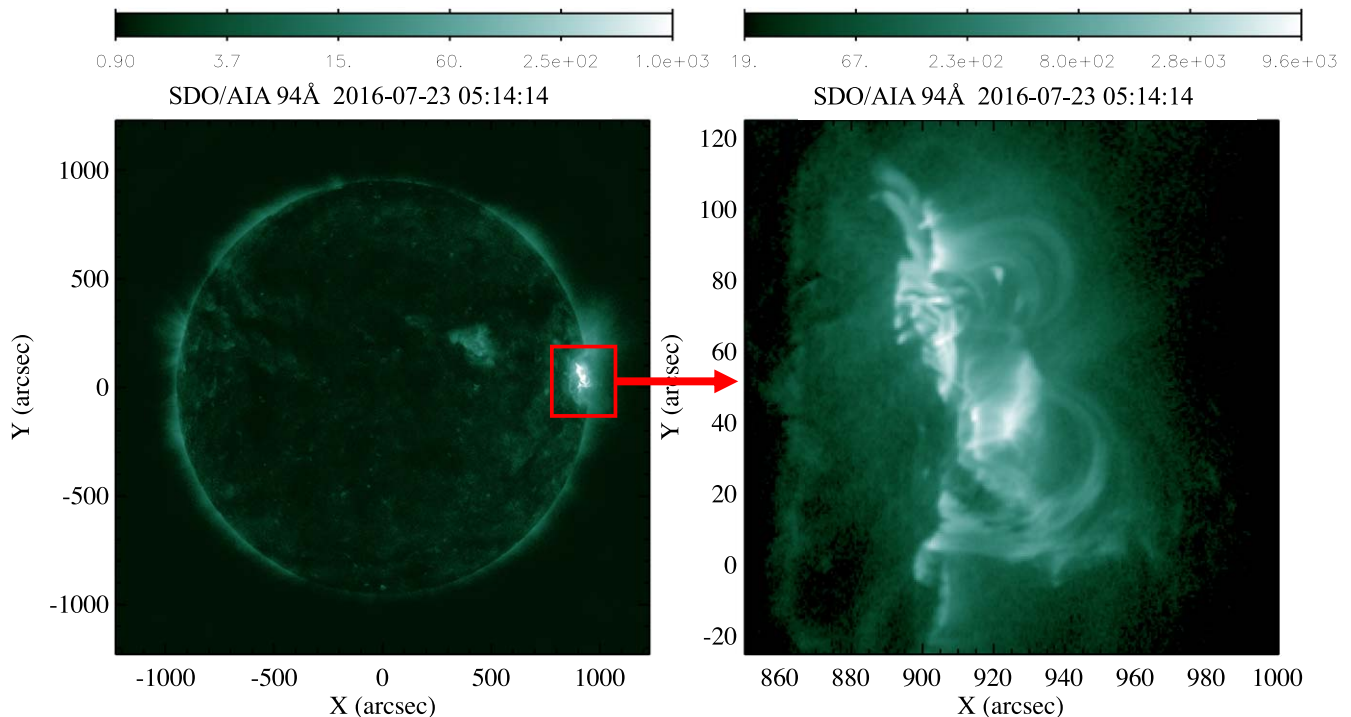


Figure 1. SDO/AIA 94 Å images of the GOES M7.6 flare at 2016-07-23 05:14:14 UT. The flare onset occurred around 05:00 UT in NOAA AR 12567 in the northern hemisphere and near the west limb (N05W73).

—which is only weakly sensitive to ionization state—is more suitable to study the detailed time evolution of these processes.

The time evolution and relationships of thermal and nonthermal emission in flares have been studied using continuum emission—bremsstrahlung (free–free) and radiative recombination (free–bound)—from the heated plasma and accelerated electrons, e.g., observed by the Reuven Ramaty High Energy Solar Spectroscopic Imager (RHESSI; Lin et al. 2002) spacecraft in hard X-rays (HXR; $E \gtrsim 10$ keV). However, RHESSI is limited in its sensitivity to the soft X-ray (SXR; $E \lesssim 10$ keV) band, which is generally dominated by thermal emission, particularly from plasma with temperatures of ~ 5 – 20 MK. During intense flares, attenuators are often inserted in front of the detectors to avoid pulse pileup and preserve sensitivity to HXRs, especially during the impulsive phase of flares (Smith et al. 2002). The absorption by attenuators makes it difficult to determine the exact shape of the low-energy spectrum and significantly increases the uncertainty of models fit to that region of the spectrum. Consequently, it is difficult to resolve a multitemperature structure, and the temperature and the emission measure of the cooler portion of the thermal emission often have to be predicated on the assumption of isothermal based on the Geostationary Operational Environmental Satellite (GOES) two-channel X-Ray Sensor (XRS) SXR photometer fluxes (White et al. 2005).

Therefore, solar SXR spectral observations with high energy resolution ($\lesssim 1$ keV FWHM) and high time resolution (< 10 s, comparable to the Alfvén timescale) are required for a precise characterization of such a multithermal structure and its relationship to nonthermal emission. However, most prior SXR observations have been carried out either with high spectral resolution only in narrow bandpasses to track specific ionization lines (e.g., using the Bragg Crystal Spectrometer on

Yohkoh) or through measurements of spectrally integrated fluxes over a large bandpass (e.g., using the XRS on GOES).

The Miniature X-ray Solar Spectrometer (MinXSS) CubeSat is the first mission that routinely archived solar flare spectral observations with high energy resolution (~ 0.15 keV FWHM) and high time resolution (10 s time cadence) in the SXR band (Mason et al. 2016; Moore et al. 2018). Utilizing MinXSS data, Woods et al. (2017) conducted a spectral analysis for an M5.0 flare that occurred on 2016 July 23 that peaked at 02:11 UT. The MinXSS spectra obtained during the flare are generally well described by a two-temperature model with a cool and a hot component. However, because MinXSS has little sensitivity to HXR emission, studying the superhot and nonthermal components at the same time requires analyzing RHESSI HXR spectra and MinXSS SXR spectra simultaneously.

In this paper, we conduct a wide-band X-ray spectral analysis using combined MinXSS SXR and RHESSI HXR data for understanding the thermal and nonthermal emissions in a solar flare. In Section 2, we summarize the observations of the target flare we analyzed. In Section 3, we introduce the data preparation to realize the wide-band X-ray spectral analysis and show the results. We also compare these results with microwave and EUV observations. Based on these results, we discuss the origins of thermal and nonthermal emission in Section 4, and we summarize our conclusions in Section 5.

2. Observations

We analyzed the GOES M7.6-class flare, which occurred starting around 05:00 UT on 2016 July 23. The flare is located in NOAA Active Region 12567 in the northern hemisphere and near the west limb (N05W73). Figure 1 shows the 94 Å EUV images of the flare during the impulsive phase taken by the Atmospheric Imaging Assembly (AIA; Lemen et al. 2012) on board SDO. AIA takes full-solar images in three UV filters and

seven EUV filters with 1.5" resolution and a cadence of 12 s. There are no other flares occurring on the Sun at this time.

This flare is the most intense event during the 1 yr observation lifetime of MinXSS, from 2016 May to 2017 May. MinXSS made spectral observations of the entire Sun (spatially integrated) with moderately high energy resolution (~ 0.15 keV FWHM) with a time cadence of 10 s in the SXR band of 0.8–12 keV (Moore et al. 2018). This flare was also observed by RHESSI, which provides spectral observations with ~ 1 keV (FWHM) resolution and rotational modulation collimator imaging with angular resolution down to $\sim 2''$ (Lin et al. 2002). The flare was observed through the thin (A1) or thick+thin (A3) attenuators during the impulsive phase of the flare to reduce the intense SXR flux. There were no flare observation data for MinXSS after 05:21 UT and for RHESSI before 05:04 UT because of the spacecraft “eclipse” time (when the satellite is in the shadow of Earth), but there are simultaneous data from both instruments in the 05:04–05:21 UT period. The XRS on GOES continuously measures solar SXR fluxes in two broad energy bands (XRS-A: 0.5–4.0 Å; XRS-B: 1.0–8.0 Å) with a time cadence of ~ 2 s (Garcia 1994). Microwave emission from the flare was observed by the Nobeyama Radio Polarimeters (NoRP; Nakajima et al. 1985), which measured total fluxes from the entire Sun at 1, 2, 3.75, 9.4, 17, 35, and 80 GHz with a time cadence of 0.1 s.

Figure 2 shows the temporal evolution of the SXR fluxes obtained by MinXSS and GOES, the HXR flux measured by RHESSI, and the microwave intensity at 17 GHz observed by NoRP. The SXR flux gradually rises from the start of the flare (05:00:06 UT), and the GOES XRS-A (0.5–4.0 Å) flux reached its peak around 05:14 UT. There are strong peaks around 05:12 UT and 05:15 UT in HXR. Continuous microwave emission is also observed during the impulsive phase. After that, the SXR and HXR fluxes gradually decrease and then spike again around 05:28 UT.

Figure 3 shows the spectral evolution in the SXR band observed by MinXSS during the flare. The detailed spectra in terms of energy and time evolution in the SXR band are obtained, and line emission from Ca XIX (3.9 keV), Fe XXV (6.7 keV, 7.8 keV), and Ni XXVII (7.8 keV) is clearly observed. Therefore, by conducting spectral analysis and separately characterizing the thermal and nonthermal emission, we can follow the evolution of the temperature and emission measures of the thermal components and the power-law index of the nonthermal emission. This information will help us to understand the mechanisms of particle acceleration and the heating and cooling processes associated with solar flares.

3. Analysis

3.1. Spectral Fitting Using MinXSS and RHESSI

We performed spectral fitting to MinXSS and RHESSI data simultaneously in the energy range of 1.5–100 keV. In this study, we utilize XSPEC (version 12.11.0; Arnaud 1996), the standard spectrum analysis tool in the field of high-energy astronomy (see Appendix A for details). The Object SPectral EXecutive (OSPEX)⁸ software package in the SolarSoftWare (SSW)⁹ IDL suite is often used for X-ray spectrum analysis in

solar physics. However, at this time, OSPEX cannot do simultaneous joint fitting of data from more than one instrument, and thus we use XSPEC, which does allow such analysis. We note that there are no flare observation data for MinXSS after 05:20:54 UT because of spacecraft “eclipse,” so spectral analysis after this time is performed using only RHESSI data.

We use the forward-modeling method in XSPEC, where an incident photon model spectrum is assumed and convolved with the instrument response to obtain a modeled count spectrum, which is then compared with the observed spectrum using the χ^2 -statistic to assess goodness of fit. The model parameters are then adjusted and the fit procedure is iterated until a minimum χ^2 value is achieved. The statistical error of each channel count value is considered in the χ^2 calculation, and the systematic error term in XSPEC is set to 0. The fit model components are the APEC isothermal emission model (`vappec`) and a broken power law (`bknpower`) for nonthermal emission. `vappec` models thermal emission from an optically thin hot plasma and is calculated based on AtomDB (Foster et al. 2012). The main parameters are a plasma temperature T and an emission measure EM. Abundance ratios (atomic number ratios of each element relative to hydrogen) for He, C, N, O, Ne, Mg, Al, Si, S, Ar, Ca, Fe, and Ni can also be set or fit. In this study, we use abundances based on Schmelz et al. (2012). `bknpower` models power-law nonthermal emission with parameters including a break energy E_{break} , power-law photon indices of γ_1 for energies below E_{break} and γ_2 for higher energies, and normalization K :

$$A(E) = \begin{cases} KE^{-\gamma_1} & (E \leq E_{\text{break}}) \\ KE_{\text{break}}^{-(\gamma_1-\gamma_2)} (E/1 \text{ keV})^{-\gamma_2} & (E \geq E_{\text{break}}) \end{cases} \quad (1)$$

Since thermal emission dominates at lower energies, the break energy E_{break} is used to model the effective low-energy cutoff of the nonthermal emission. The spectral index below the break energy, γ_1 , is held fixed at 2, and the other parameters are fitted.

The observed spectra are spatially integrated and therefore contain a background component. It is necessary to subtract this background to isolate the flare emission for spectral analysis. To subtract nonsolar X-ray background (NXB), which is mainly caused by bremsstrahlung from cosmic rays and charged particles interacting in the spacecraft, the NXB is evaluated by using spectral data during spacecraft “eclipse.” The NXB of MinXSS is negligible but is significant for RHESSI, and we thus time-average the spectra during the eclipse time of 04:54–05:02 UT and subtract this from the flare observations. The solar emission before the flare is treated as a “pre-flare” background. This emission can be interpreted as X-rays emitted from the entire surface of the Sun other than the target solar flare. To isolate the flare emission, a time-average spectrum before the start of the flare, integrated over 04:45:54–04:57:34 UT, is fixed as a “pre-flare component” and incorporated into the model (added to the model flare emission) when conducting spectral analysis. While such background components can often vary in time for other flares, our assumption of a constant summed background is supported by the RHESSI light curves during eclipse and post-flare intervals (e.g., Figure 2).

Figure 4 shows the results of spectral fitting during the peak of the flare (05:15:04–05:15:14 UT) using both “MinXSS and RHESSI” and “only RHESSI” spectra. With RHESSI alone,

⁸ http://hesperia.gsfc.nasa.gov/ssw/packages/spex/doc/ospex_explanation.html

⁹ https://www.lmsal.com/solarsoft/ssw_install.html

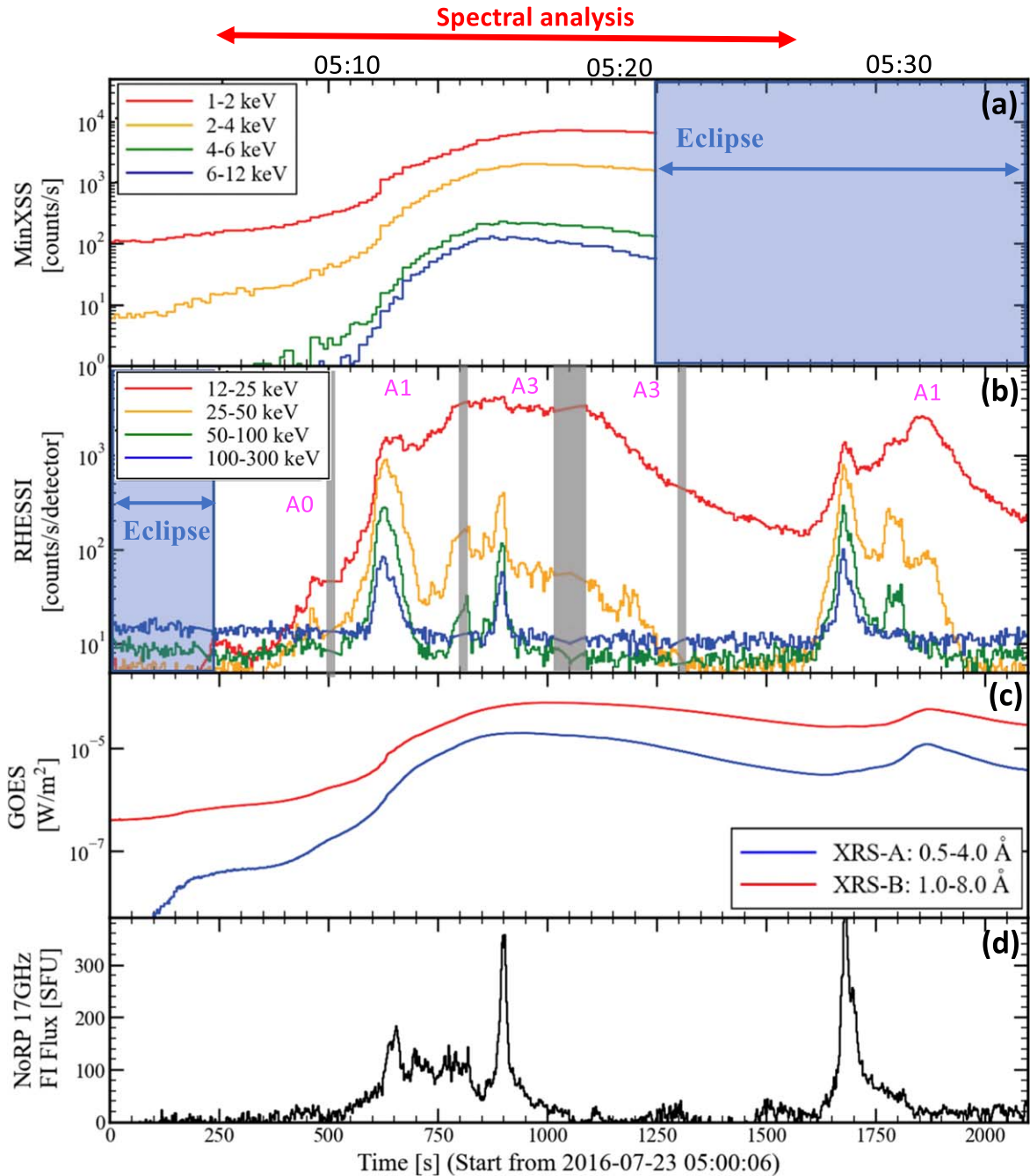


Figure 2. Multiwavelength light curves of the 2016 July 23 M7.6 solar flare. (a) SXR MinXSS count rates in 10 s time bins and several energy bands, as marked. (b) HXR RHESSI corrected-count rate in 4 s time bins and several energy bands, as marked. The A0, A1, and A3 labels represent the attenuator state (Smith et al. 2002), the effects of which have been deconvolved from the light curves. (c) SXR GOES fluxes in 2 s time bins for the short (XRS-A; 0.5–4.0 Å) and long (XRS-B; 1.0–8.0 Å) wavelength channels. (d) Microwave NoRP flux $I(R + L)$ at 17 GHz with the average pre-flare flux subtracted. The blue-highlighted times for MinXSS and RHESSI indicate spacecraft “eclipse” (when the satellite is in Earth’s shadow), and the gray-highlighted time intervals for RHESSI indicate switching between attenuate states, which are excluded from this study, as the detector responses are not well defined during these periods.

the nonthermal power law and the thermal emission from a “hot” ($T \approx 15$ MK) and a “superhot” plasma ($T \approx 30$ MK) are detected. However, these two thermal components are poorly constrained and can “trade off” with each other because of lack of sensitivity at lower energies, especially when the flare is in the impulsive phase and RHESSI is in attenuator state A3. In contrast, with the addition of MinXSS spectra in the SXR band, the multithermal structure is resolved. Three thermal

components—a “cool” plasma ($T \approx 3$ MK), a “hot” plasma, and a “superhot” plasma—and a nonthermal power-law component are detected and constrained at the same time by simultaneously fitting “MinXSS and RHESSI” spectra.

Figure 5 shows the results of spectral fitting for each time interval using MinXSS and RHESSI, and the time evolutions of the parameters of each of the thermal and nonthermal components are summarized in Figure 6. The behavior of

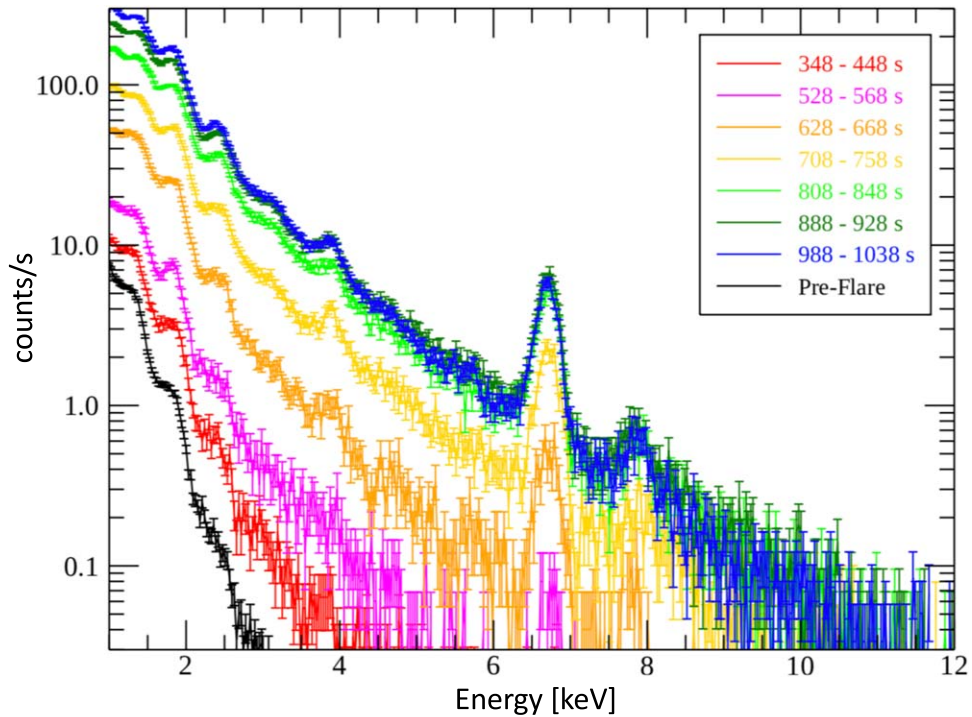


Figure 3. Spectral evolution of the 2016 July 23 M7.6 solar flare observed by MinXSS. The time labels indicate the elapsed time from 2016-07-23 05:00:06 UT. The pre-flare spectrum before the start of the flare (04:45:54–04:57:34 UT) is also shown.

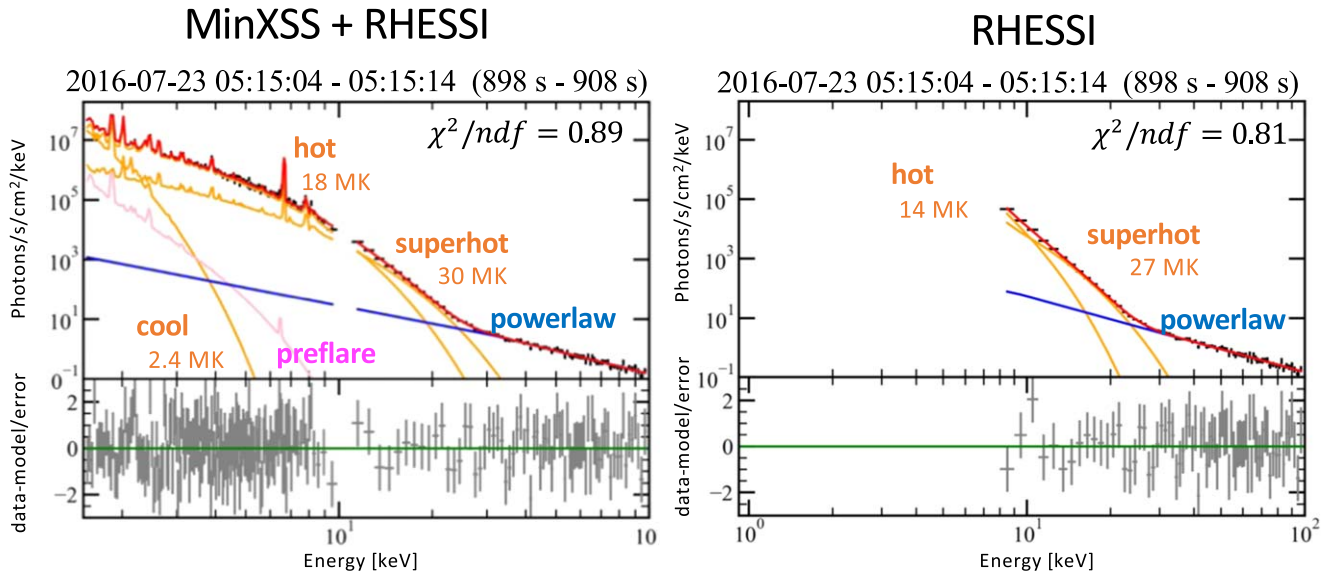


Figure 4. Spectral fitting for the 2016 July 23 M7.6 solar flare during 05:15:04–05:15:14 UT, using MinXSS and RHESSI combined spectra (left) and with only the RHESSI spectrum (right). The addition of MinXSS SXR observations enables the multithermal structure to be clearly resolved.

thermal and nonthermal emission in each flare phase is summarized in Table 1. The comparison of the multitemperature fitting model is shown in Appendix B, for complete details.

Even as early as the pre-impulsive phase of the flare (spectrum A, B), isothermal emission alone is not sufficient to explain the observed spectrum. A cool thermal component ($T \approx 6$ MK) is also observed in addition to the hot thermal emission ($T \approx 18$ MK), which is inferred from the observed GOES fluxes, and a nonthermal component is also required at higher energies. In the first impulsive phase, as the HXR flux peaks and the nonthermal emission becomes harder, with $\gamma_2 \approx 2.8$ (spectrum C), the emission measures of the hot and

cool thermal emission increase drastically by more than hundreds of times. In addition, the temperature of cool plasma appears to decrease slightly to $T \approx 3$ MK. During the interval of the two impulsive phases of the flare, the nonthermal emission softens (higher γ_2), and the superhot thermal emission ($T \approx 30$ MK) gradually appears (spectrum D). In the second impulsive phase, the spectral index γ_2 hardens as the HXR flux rises and then softens again as the HXR flux decreases. This soft–hard–soft (SHS) behavior of nonthermal emission has been reported in other solar flares (e.g., Benz 1977; Kosugi et al. 1988). The HXR flux then peaks again, and the nonthermal emission becomes the hardest, with $\gamma_2 \approx 2.6$ (spectrum E). In the decay

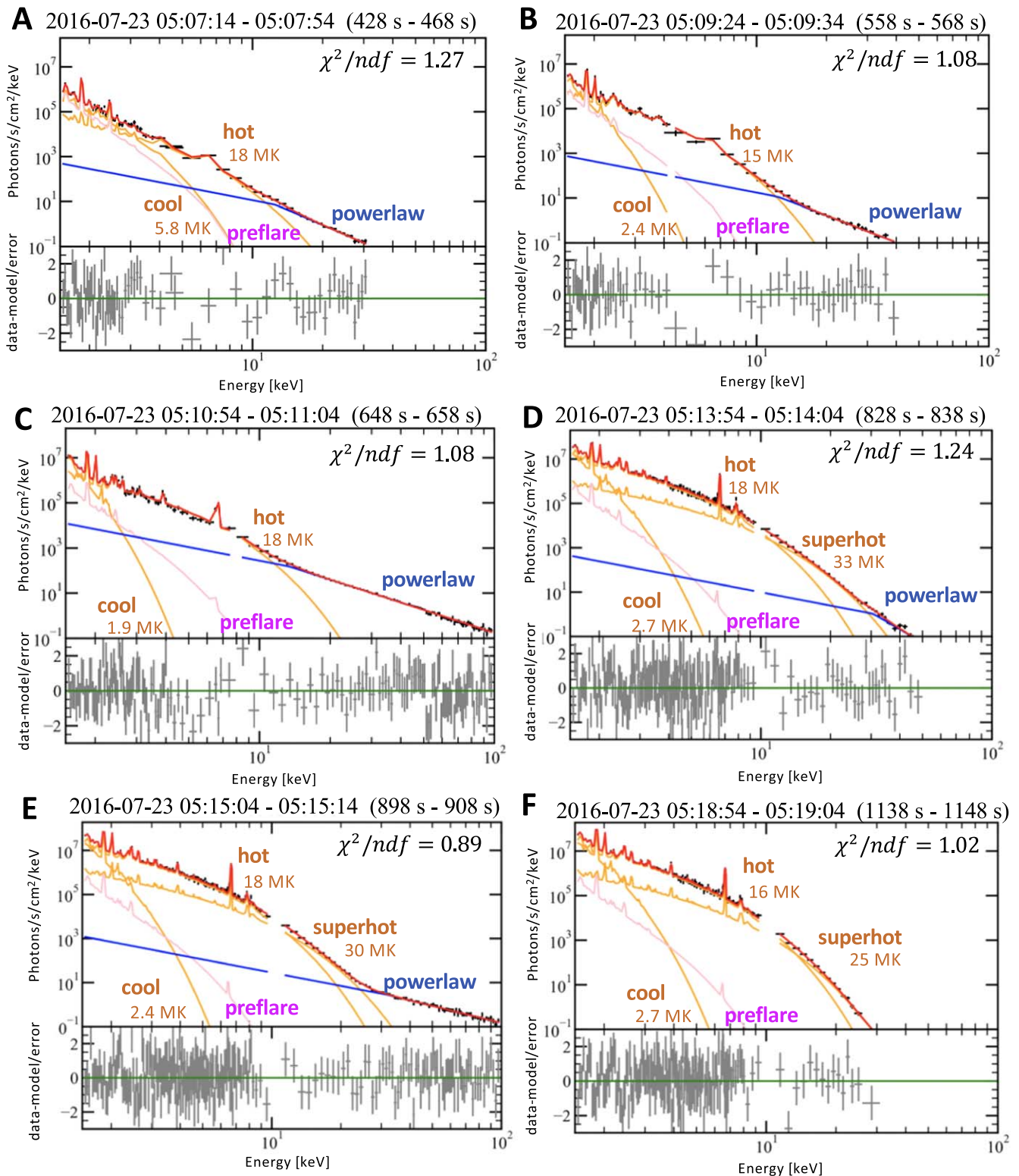


Figure 5. Spectral evolution of the 2016 July 23 M7.6 solar flare using combined MinXSS SXR and RHESSI HXR spectra. The A–F labels correspond to the time intervals marked in Figure 6. The pink spectrum represents the (fixed) pre-flare background. The blue curve represents the nonthermal emission (fit as a broken power law). The orange curve represents the thermal emission, and three temperatures are fit within the model: cool (~ 3 MK) and hot (~ 17 MK) components observed throughout the flare, and a superhot (~ 30 MK) component starting around 05:11 UT. The red curve represents the sum of all model components: the pre-flare, thermal, and nonthermal components. An animation of the spectral evolution of the 2016 July 23 M7.6 solar flare is available in the online journal. The animation proceeds from 05:04:34 to 05:20:14 UT; the animated images are not annotated.

(An animation of this figure is available.)

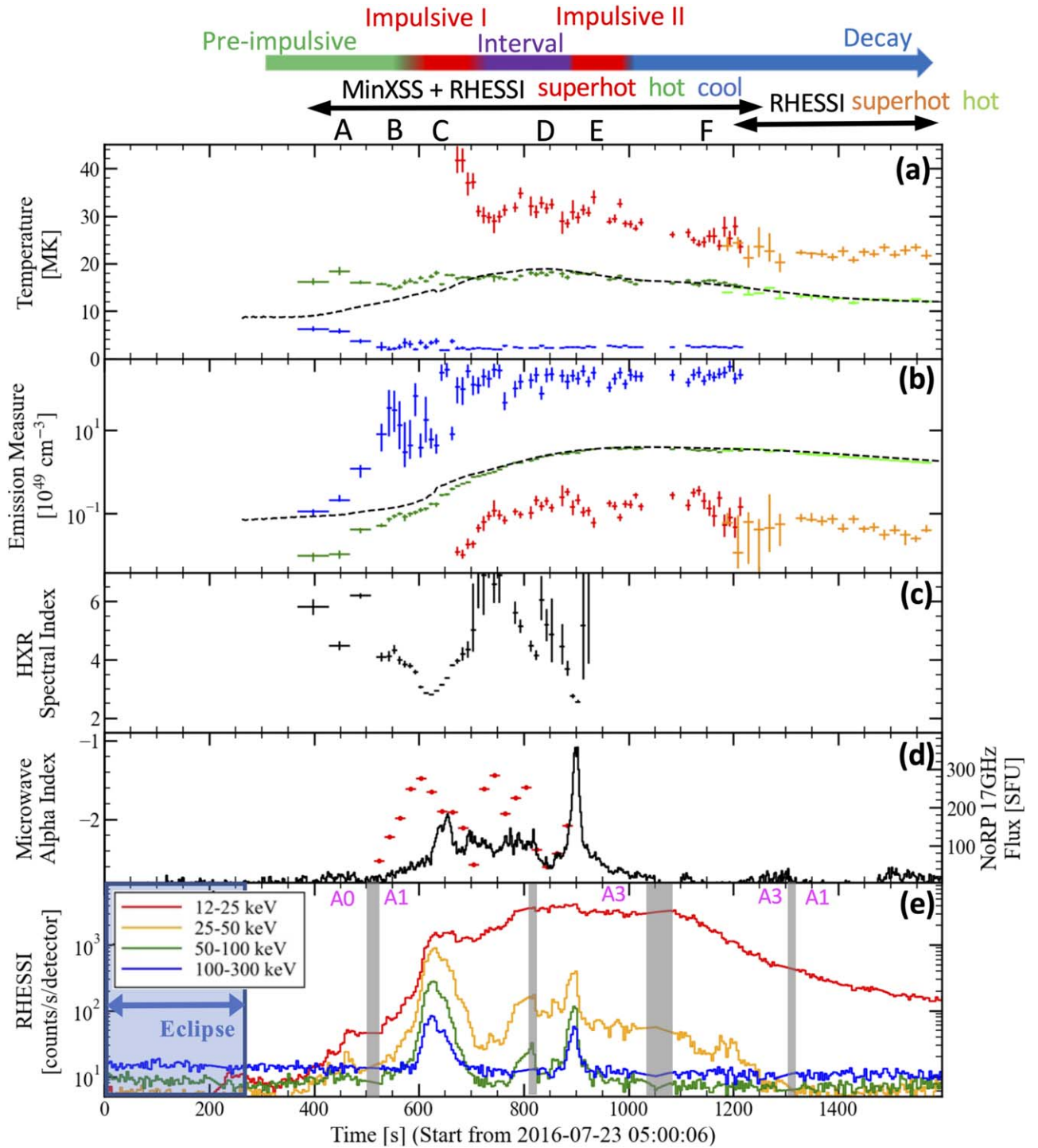


Figure 6. Temporal evolution of thermal and nonthermal emission from spectral analysis. (a) Temperature and (b) emission measure of each fit thermal component. The black dotted curve represents the isothermal temperature and emission measure calculated from GOES two-channel fluxes (White et al. 2005). (c) HXR spectral index of the nonthermal component above the break energy. (d) Spectral index of the NoRP microwave spectra above the turnover frequency (red) and NoRP 17 GHz flux (black). (e) HXR RHESSI corrected-count rate, for reference. Error bars in panels (a)–(c) are 1σ , determined from the fit routine.

phase of the flare, the nonthermal emission fades and the temperatures of the hot and superhot thermal emissions gradually cool (spectrum F).

3.2. Comparison of Fitting Results with GOES Flux

In order to check the consistency of our fitting results using MinXSS and RHESSI with measured GOES fluxes, we

estimated the X-ray fluxes that would be expected to be observed by GOES based on the spectral fits. Then, we compared these estimated fluxes with those actually observed by GOES.

First, the incident photon flux in units of $[\text{W m}^{-2}]$ is calculated based on the fit parameters for each time interval in Figure 6 (e.g., see the red spectral curves in Figure 5, which are then converted to W m^{-2}). Then, the incident photon flux in

Table 1
Time Evolution of Thermal and Nonthermal Emission of the GOES M7.6-class Flare

	Thermal Emission Soft X-Ray	Nonthermal Emission		
		Hard X-Ray	Microwave (17 GHz)	Spectrum
Pre-impulsive phase	Cool (~ 6 MK) and hot (~ 18 MK) plasma components are detected.	The nonthermal power-law component is detected.	The flux is not detected.	A, B
Impulsive phase I	The emission measures drastically increase ($> \times 100$).	The flux peaks and the power-law index becomes hard, $\gamma_2 \approx 2.8$.	The flux gradually increases and peaks.	C
Interval phase	Superhot (~ 30 MK) plasma component gradually appears.	Only small subpeaks are detected.	The flux is continuously emitted.	D
Impulsive phase II	The emission measures continuously increase.	The flux peaks again and becomes the hardest, $\gamma_2 \approx 2.6$.	The flux strongly peaks.	E
Decay phase	The temperatures of the hot and superhot plasma components gradually cool, and the emission measures also decrease.	The nonthermal power-law component fades.	The flux is not detected.	F

8

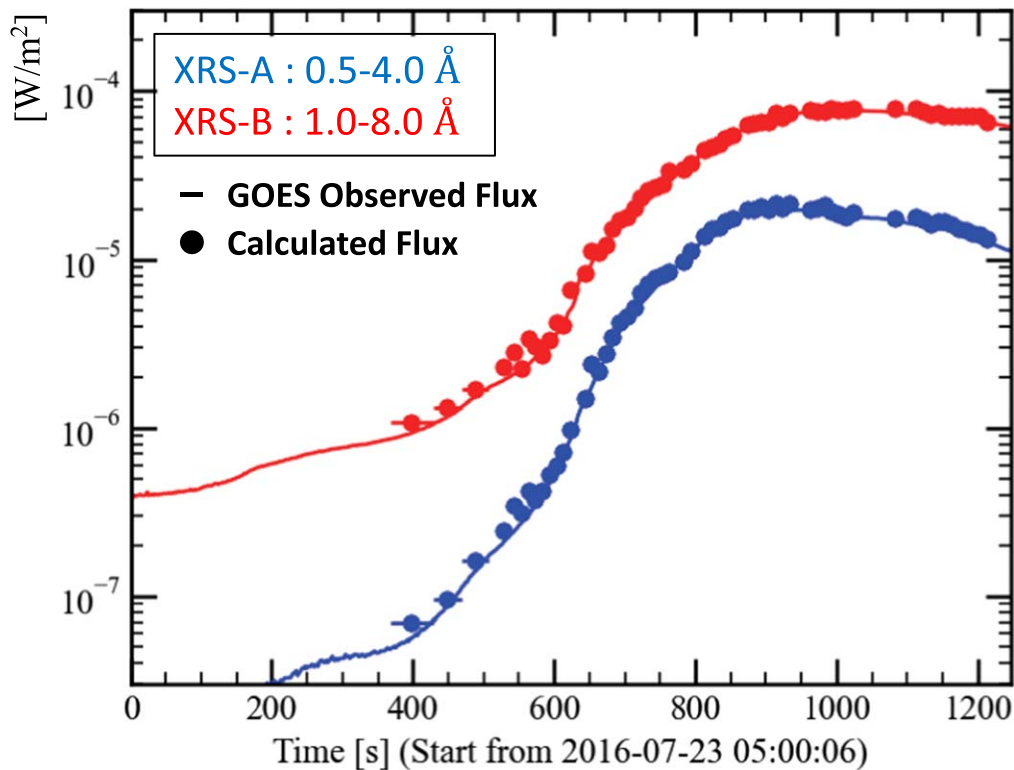


Figure 7. Comparison of fluxes estimated from the results of spectral analysis to those actually observed by GOES. The model-estimated fluxes are in good agreement with the GOES observations.

each energy is converted to the current $I(E)[A]$ in the GOES ionization chamber by folding it through the wavelength-dependent response of GOES (the transfer function; see Tables 6 and 7 of Machol & Viereck 2016). The current at each energy $I(E)[A]$ is summed for all energies to obtain the total current, $I_{\text{total}}[A]$. Then, we divide the total current by the scalar flux conversion factor $C [A (W m^{-2})^{-1}]$ (XRS-A: 1.342×10^{-2} ; XRS-B: 5.703×10^{-6} ; this includes the “SWPC scaling factor”; see Table 5 of Machol & Viereck 2016) to estimate the expected GOES flux $[W m^{-2}]$.

Figure 7 shows the estimated GOES fluxes from the results of spectral analysis and the actually observed GOES fluxes. The estimated fluxes are consistent with the GOES observations throughout the flare. It should be noted that MinXSS and RHESSI data represent qualitatively different information compared with GOES. For GOES, with two broad channels, it is only possible to calculate the time evolution of the temperature and emission measure based on the observed fluxes in Figure 7 under the assumption of isothermal emission, and abundances must be assumed, typically as coronal (White et al. 2005). Therefore, this single temperature and emission measure just represents the averaged behavior of the thermal emission, like the dashed black curves in panels (a) and (b) of Figure 6. In contrast, by using MinXSS and RHESSI data, we can resolve the multitemperature structure of the thermal emission, as well as the nonthermal emission, and we can follow the time evolution of each component individually, like the colored measurements in Figure 6.

3.3. Microwave Spectral Analysis

Microwave emission is observed during the flare by NoRP at frequencies from 1 to 34 GHz, and we analyze its spectral

evolution. We fit the NoRP spectra at frequencies of 2, 3.75, 9.4 and 17 GHz, with an integration time of 20 s, with a generic model function (see Equation (C1) in Appendix C) during 05:08:49–05:14:49 UT, and we determined the spectral index α_H above a turnover frequency $\widehat{\nu}_T$ for each time interval; the fit results for the spectral index are summarized in panel (d) of Figure 6. During the fitting time interval, the turnover frequency $\widehat{\nu}_T$ is less than 17 GHz, and a negative spectral index ($-2.8 < \alpha_H < -1.4$) is determined at higher (optically thin) frequencies.

We also estimated the contribution of bremsstrahlung emission based on the temperatures and emission measures obtained by the X-ray spectral analysis using an optically thin regime for hot and superhot plasma and an optically thick regime for cool plasma. The area of the cool plasma emission region estimated from the AIA 335 Å image (95% contour regions) is $A \approx 100 Mm^2$. Therefore, the density of the cool plasma is estimated to be $n_e \approx EM/A^{3/2} \approx 10^{12} cm^{-3}$, which is dense enough to be optically thick ($\tau \approx 100$ for 17 GHz). In the impulsive phase, the observed flux by NoRP at 17 GHz is ~ 140 SFU, while the contribution of the bremsstrahlung emission is estimated to be less than 30 SFU and can be negligible.

Therefore, the continuous microwave emissions observed at 17 GHz must be optically thin gyrosynchrotron emission from mildly relativistic nonthermal electrons (Dulk 1985; Bastian et al. 1998).

3.4. Imaging and DEM Analysis

To explore the locations of the thermal and nonthermal emission, we conducted an imaging analysis. Using the six EUV filtergram observations of AIA with peak temperature

Image: SDO/AIA 94 Å Contour: RHESSI 6–10 keV 18–25 keV 35–80 keV

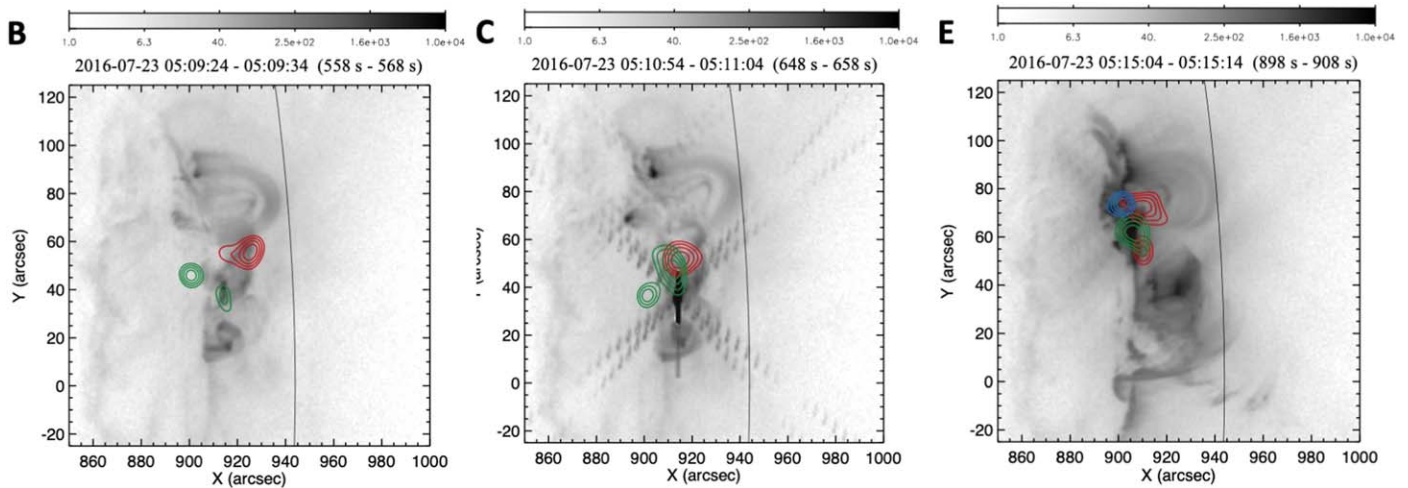


Figure 8. SDO/AIA 94 Å image (gray scale) overlaid with RHESSI HXR contours at 60%, 70%, 80%, and 90% of the peak intensity in the energy ranges of 6–10 keV (red), 18–25 keV (green), and 35–80 keV (blue). The AIA 94 Å emission corresponds primarily to plasma of ~ 6 MK. The B, C, and E labels correspond to the time intervals shown in Figure 6. RHESSI image synthesis was performed using the “Clean” method (Hurford et al. 2002) using grids 3 and 8. Image synthesis at 35–80 keV is omitted in the left and middle panels owing to poor statistics at those times.

sensitivity above 1 MK (94, 131, 171, 193, 211, and 335 Å, corresponding to Fe lines from different ion species; Boerner et al. 2014), the temperature distribution or DEM can be calculated by solving the relationship between the temperature response $K_i(T)$ in the i th filter and the count rate y_i observed in the i th filter of AIA:

$$y_i = \int_T K_i(T) \text{DEM}(T) dT. \quad (2)$$

Here $\text{DEM}(T)$ is the DEM integrated along the line of sight to the observer:

$$\text{DEM}(T) dT = \int n_e^2(T) dz \quad [\text{cm}^{-5}], \quad (3)$$

where $n_e(T)$ is the thermal electron number density at temperature T . In this study, we used the regularization method of Hannah & Kontar (2012) to calculate the DEM in each pixel to identify the locations of cool thermal emission ($T = 3 - 4$ MK). Figure 9 shows the results of the 3–4 MK temperature bin of the DEM calculation at the beginning of the flare (05:06:36 UT) and at the end of the flare (05:15:48 UT). The time evolution clearly shows that the 3–4 MK plasma increases in the flaring loop.

We note that while AIA data can be used for DEM analysis in this way, the AIA response has poor sensitivity above ~ 10 MK, particularly for the high flare temperatures observed here, and we therefore used AIA primarily to locate the cooler emission where the AIA response is strong. While AIA data could potentially be combined with the joint MinXSS–RHESSI data to further enhance the joint-instrument DEM analysis (e.g., Caspi et al. 2014; Inglis & Christe 2014; Moore 2017), such techniques are significantly complex and require careful consideration of the limitations of each instrument, and thus they are beyond the scope of this work.

RHESSI uses a rotational modulation collimator to obtain spatial information, and the location of the X-ray emission on the Sun is calculated using an image synthesis method from flux modulations observed as the spacecraft rotates. In order to locate the hot ($T \approx 15$ MK) and superhot ($T \approx 30$ MK) thermal

components and the nonthermal component, RHESSI image synthesis was performed using the “Clean” method (Hurford et al. 2002) available in SSW using imaging grids 3 and 8. The integration time was 40 s, and the energy bands were 6–10 keV, 18–25 keV, and 35–80 keV. The 6–10 keV band is dominated by the hot thermal component, the 18–25 keV band has contributions from the nonthermal and (when present) the superhot component, and the 35–80 keV band shows the nonthermal component only. The AIA 94 Å images (emitted by Fe XVIII, corresponding to the plasma temperatures of 6 MK) with RHESSI contours overlaid are presented in Figure 8. The B, C, and E labels correspond to the time intervals shown in Figure 6.

At the beginning of the flare (time interval B), we can see the two footpoint HXR sources (18–25 keV) that correspond to the nonthermal thick-target bremsstrahlung when the accelerated electrons impact the chromosphere. The peak of the HXR emission (time interval C) shows a dramatic increase in the HXR footpoint emission (18–25 keV), and most of the hot thermal emission (6–10 keV) is now lower in the loop. After the HXR peak (time interval E), the emission region shifts from the south to the north, with an apparently different set of loops being energized and an additional source of hot emission (6–10 keV) appearing along with a new HXR footpoint (35–80 keV) and the superhot thermal component (18–25 keV). We note that microwave imaging using the Nobeyama Radioheliograph (NoRH; Nakajima et al. 1994) is not shown because the solar disk used for alignment and the flare microwave source could not be scaled simultaneously, and it is thus difficult to reliably compose the microwave image for this event.

4. Discussion

By conducting simultaneous fitting using MinXSS and RHESSI spectra observed in the M7.6 flare that occurred on 2016 July 23, it becomes possible to clearly resolve a nonthermal power-law component and multiple thermal components (a cool plasma at $T \approx 3$ MK, a hot plasma at $T \approx 15$ MK) and a superhot plasma at $T \approx 30$ MK) and to

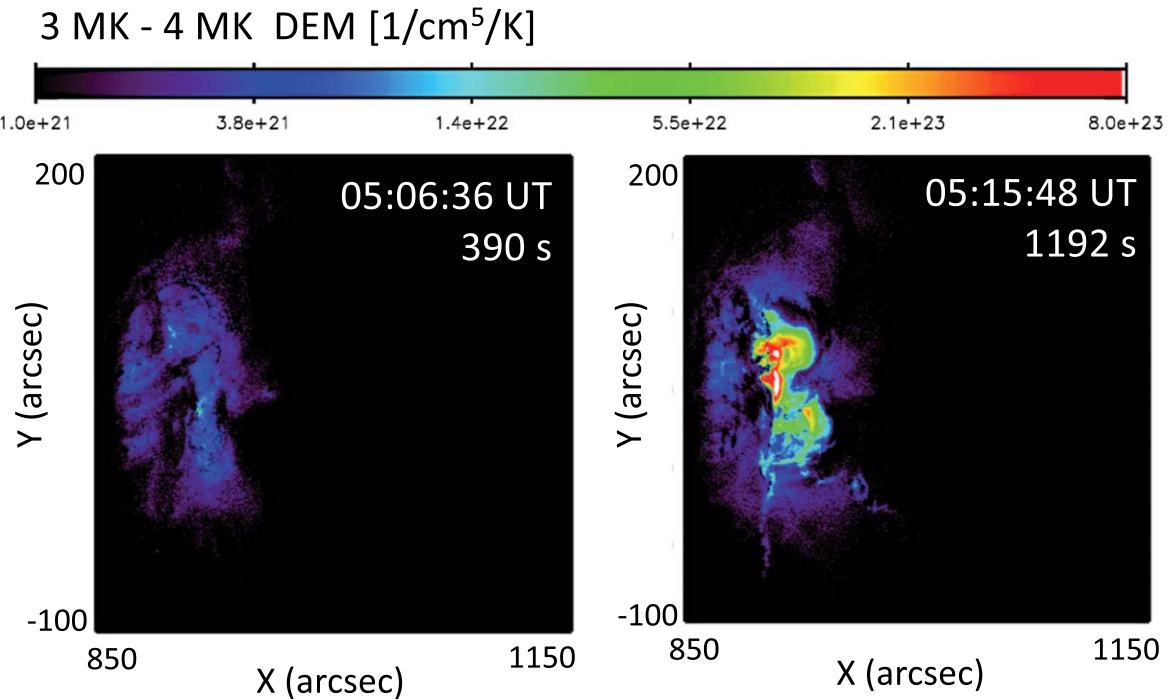


Figure 9. Results of the AIA DEM calculation using the regularization method of Hannah & Kontar (2012) at the beginning (05:06:36 UT) and end (05:15:48 UT) of the flare. Here we use the six EUV filters with peak temperature sensitivity above 1 MK (94, 131, 171, 193, 211, and 333 Å). Only the 3–4 MK temperature bin is shown. The DEM of 3–4 MK plasma clearly increases within the flaring loop.

follow their time evolution with a cadence of 10 s, which also corresponds to the Alfvén timescale in the solar corona. From the beginning of the flare, both the cool and hot thermal components are required to explain the observed spectra—a single isothermal is not sufficient. As the nonthermal spectrum increases and hardens, the emission measures of both the hot and cool thermal components drastically increase, and images show that the cool plasma (3–4 MK) is confined to and increasing within the flaring loop. After that, the nonthermal emission softens, and the superhot thermal emission ($T \approx 30$ MK) gradually increases, while continuous microwave emission—optically thin gyrosynchrotron emission from mildly relativistic nonthermal electrons—is observed simultaneously. Subsequently, the HXR flux peaks a second time, and the nonthermal emission hardens to its minimum spectral index of $\gamma_2 \approx 2.6$. Finally, as the nonthermal emission fades, each thermal emission gradually cools. The spectral analysis using MinXSS and RHESSI reproduces well the observed GOES SXR fluxes, providing confidence in the fit results.

This detailed time evolution information is a key to understanding the origins each spectral component. In particular, the emission measure of the cool thermal component drastically increases by more than two orders of magnitude in ~ 300 s, and the temperature appears to decrease during the first HXR peak from Figure 6. The presence of cool thermal emission in solar flares was also noted by Dennis et al. (2015). From their spectrum obtained by the Solar Assembly for X-rays on MESSENGER during the 2007 June 1 M2.8 class flare, in the energy range of 1.5–8.5 keV, they reported that the spectrum was well described by both hot and cool thermal components and observed a similar drastic increase in emission measure and slight decrease in temperature for their cool plasma. However, their results were obtained from spectra with a cadence of about 5 minutes. In contrast, through simultaneous observations and analyses of MinXSS and RHESSI spectra, we

can track temperatures and emission measures with much higher cadence, every 10 s, for both the hot and cool thermal components.

EUV imaging analysis shows that the DEM of 3–4 MK plasma, corresponding to the cool component in our spectral analysis, increases within the flaring loop (Figure 9). This implies that the cool thermal component corresponds to plasma that fills the flaring loop associated with chromospheric evaporation. Similarly, the emission measure of the hot thermal component also drastically increases, by two orders of magnitude in ~ 300 s, and is therefore also likely due to chromospheric evaporation. Many prior analyses of GOES fluxes, RHESSI HXR, and EUV Doppler-shift observations (e.g., Holman et al. 2011, for reviews) have discussed chromospheric evaporation for hot plasma ($T = 10$ –20 MK). However, by conducting SXR and HXR spectra analysis simultaneously, it is possible to reveal the multithermal structure of chromospheric evaporation including the cool plasma ($T \approx 3$ MK) together with the hotter components, self-consistently. Yokoyama & Shibata (1998) conducted MHD simulations and suggested the presence of a cool plasma ($T = 3$ –6 MK) for the large-scale flare events such as the arcade reformation associated with the prominence eruption. Milligan & Dennis (2009) also found blueshifts of Fe XIV–XXIV line emission (~ 2 –16 MK) in a flare, which is indicative of evaporated material at these temperatures. These studies are consistent with our evaporative interpretation of the cool thermal component.

The relationships between the evolution of the superhot plasma and the microwave and HXR emissions are key to elucidating the potential origins of the superhot plasma. During the interval phase (spectrum D), we found that the emission measure of the superhot plasma increased simultaneously with the continuous gyrosynchrotron emission at microwave frequencies. Since gyrosynchrotron emission is radiated from

mildly relativistic nonthermal electrons in the presence of a magnetic field, this correlation implies that the superhot component may originate from thermalization of the non-thermal electrons trapped in the corona, within the flaring loop. Similarly, the HXR emission, which implies chromospheric energy deposition by accelerated electrons, shows only small subpeaks, consistent with the microwave-generating electrons being largely trapped and not precipitating significantly into the chromosphere at this time. Moreover, in the decay phase, as the microwave emission decreases, the temperature of the superhot plasma gradually cools, and the emission measure also decreases. Caspi & Lin (2010) found that, for their flare, the hot and superhot plasmas were spatially distinct, separated by $\sim 11''$ based on RHESSI imaging, and suggested that significant heating of superhot plasma occurs directly in the corona. A more detailed analysis by Caspi et al. (2015) found that the superhot emission was also cospatial with apparent nonthermal emission for some time, indicating a potential link between superhot plasma and nonthermal electrons accelerated in the corona. Our microwave results support that interpretation.

We note that Cheung et al. (2019) suggested that adiabatic compression and viscous dissipation create a superhot plasma with temperatures exceeding 100 MK at a higher altitude than hot plasma loop tops, based on MHD simulations. Caspi et al. (2015) also found that the superhot source was at higher altitudes than the hot plasma, although cooler (~ 40 MK) than suggested by Cheung et al. (2019). In this flare, however, the apparent superhot emission (18–25 keV contours in the right panel of Figure 8) appears to be at similar or possibly even lower altitude than the hot emission (6–10 keV contours in that figure), although this is somewhat complicated by the nonthermal contribution to the 18–25 keV contours and by the more complex flaring geometry, with multiple loop systems being energized. A “thermal imaging” analysis to more cleanly separate the emission sources by combining the spectral and spatial information (as in Caspi et al. 2015) may yield further insight and will be the subject of a future paper.

Since the dynamic range of RHESSI imaging is only about ~ 10 , it is hard to distinguish X-ray sources that are ~ 10 times weaker than the brightest points, e.g., to distinguish weak coronal emission in the presence of bright chromospheric emission. While our speculation on the origins of the superhot plasma are consistent with observations and prior interpretation, truly confirming the origin of superhot plasma requires imaging spectroscopic observation with significantly improved dynamic range in both the SXR and HXR ranges. Elemental abundances are also valuable tracers of plasma origins (e.g., Warren 2014; Laming 2021), but many of the relevant lines (e.g., Fe XXV) have a broad temperature response and will therefore contain contributions from both hot and superhot plasmas, which can be difficult to distinguish in spatially integrated spectra. The Focusing Optics X-ray Solar Imager (FOXSI; Krucker et al. 2009) sounding rocket experiment demonstrated solar spectroscopy from directly focused HXR observations. The upcoming FOXSI-4 launch (Glesener et al. 2020; Buitrago-Casas et al. 2021) will be specifically timed during a solar flare, achieving a much better dynamic range of up to ~ 100 times larger than RHESSI to provide simultaneous diagnostics of spatially separated coronal and chromospheric emission. Future photon-counting imaging spectrometers coupled with high-resolution focusing optics, in both SXR

and HXR bands such as from the satellite mission concept Physics of Energetic and Nonthermal plasmas in the X (= magnetic reconnection) region (PhoENiX; Narukage 2019), will enable us to follow the spectral evolution from different regions. This would be even further improved with higher spectral resolution across a wide band, to provide abundance diagnostics from a variety of elements (e.g., Fe, Ca, Si, Mg, O, Ne, Ar) across a broad range of coronal temperatures, such as would be provided by instruments like the Marshall Grazing Incidence X-ray Spectrometer (MaGIXS; Kobayashi et al. 2018; Athiray et al. 2019) and the CubeSat Imaging X-ray Solar Spectrometer (CubIXSS; Caspi et al. 2021), for additional constraints on plasma heating mechanisms. With such observations, it will be possible to verify and/or improve the interpretations of the origins of each thermal component we obtained from this study by directly comparing the emissions and their time evolution from the flaring loop, including footpoints and loop top, and any other relevant sources.

5. Conclusion

In summary, we have conducted a wide-band X-ray spectral analysis using combined SXR spectra from MinXSS and HXR spectra from RHESSI simultaneously. This joint analysis revealed a nonthermal component and three-temperature multithermal component—“cool” ($T \approx 3$ MK), “hot” ($T \approx 15$ MK), and “superhot” ($T \approx 30$ MK)—with most of these components present throughout the flare. In addition, we followed the time evolution of the thermal and nonthermal emissions with 10 s cadence, which corresponds to the Alfvén timescale in the solar corona. The time evolution of the spectral components and an imaging DEM analysis suggest that the cool and hot thermal components both correspond to plasma filling the flaring loop associated with chromospheric evaporation. On the other hand, a correlation between the superhot thermal time evolution and microwave emission from non-thermal electrons suggests that the superhot component could be explained by thermalization of the nonthermal electrons trapped in the flaring loop. Following the time evolution of the multitemperature structure of the spectra using MinXSS and RHESSI provides new insights into the possible origins of these thermal emissions. However, it is necessary to follow the time evolution of the spectra in each emission region, with improved dynamic range in each spatial region, to elucidate the origin of the superhot thermal component and its relationship with nonthermal emission. In the future, direct-focusing SXR and HXR observations such as from FOXSI-4 and PhoENiX will allow us to observe a wide dynamic range and track spectral evolution region by region. By accumulating such observations, we will be able to clarify the origin of each thermal and nonthermal emission component and their relationship, which will help us understand the particle acceleration and resolve the complex energy conversion system associated with magnetic reconnection.

The authors would like to thank Christopher S. Moore for providing the response matrix of the MinXSS silicon drift detector (X123-SDD). The authors also thank Lindsay Glesener and Julie Vievering for their helpful discussions. This work was supported by JSPS, Japan KAKENHI grant Nos. 17K14314, 18H03724, 18H05457, 20H00153, 21KK0052, 22H00134, and 22J12583. This work was also supported by FoPM (WINGS Program) and JSR Fellowship, the University of Tokyo, Japan. This work was

carried out by the joint research program of the Institute for Space-Earth Environmental Research, Nagoya University. A.C. and T.N. W. were supported by NASA grant NNX17AI71G, and A.C. was also partially supported by NASA grant 80NSSC19K0287.

Appendix A XSPEC Format and Data Preparation

XSPEC (version 12.11.0; Arnaud 1996) is the standard spectrum analysis tool in the field of high-energy astronomy. To perform fitting using XSPEC, the following Flexible Image Transport System (FITS) files are required:

1. Spectrum PHA data file (PHA file):

The observation data (detected counts and statistical/systematic errors in each channel of the detector) and auxiliary information required during the spectral analysis process (live time, observation time, the related background and response files, etc.).

2. Redistribution matrix file (RMF):

Information on nominal energy range in each channel of the detector and a two-dimensional matrix (redistribution matrix). The redistribution matrix (also sometimes called a “detector response matrix”) represents the probability that an incident photon with energy E will be detected in a certain channel i , accounting for potential energy loss or gain effects due to energy resolution, escape peaks, Compton scattering, etc.

3. Ancillary response file (ARF):

One-dimensional vector as a function of energy describing the effective area, such as filter transmission and detection efficiency of the detector.

All of the above files must be created according to the OGIP standard data format described in Arnaud et al. (2009) and George et al. (2007). For solar observations, detector response information corresponding to the RMF and ARF is often already convolved into one two-dimensional data file and can be loaded as a single “response file” in XSPEC.

We created the PHA files and response files based on MinXSS and RHESSI data through the following procedure. For MinXSS, the spectral data can be directly downloaded from the MinXSS website. Various levels of data are prepared in IDL “sav” file format, depending on the desired stage of data processing. In this analysis, we used “Level 0D” data,¹⁰ which include raw detector count data along with the ancillary information (measurement time, satellite position, etc.) required for calibration and processing to higher levels. The spectrum, observation time, and integrated live-time

information were extracted from the IDL sav file, and the FITS files were created according to the OGIP data format. For RHESSI, a dedicated software package is available within the IDL-based integrated solar analysis software SolarSoftWare (SSW) distribution, providing complete access to the data and all processing tools. The observation time, energy range, and energy binning were specified in calls to the software to generate appropriate spectrum and response data. The FITS files produced by the RHESSI SSW package are designed to be compatible with OSPEX, the standard spectral analysis tool in SSW, and this format is not directly compatible with XSPEC. Therefore, we converted these FITS files to the OGIP data format for ingestion into XSPEC.

Appendix B Comparison among the Multitemperature Model Fitting

Figure 10 shows the “isothermal” and “two-temperature” thermal emission models with nonthermal power-law model fits to the observed MinXSS and RHESSI count flux spectra for the 2016-07-23 05:10:54–05:11:04 UT period (time interval C in Figure 6). The fitting is performed over the 1.5–100 keV energy range, and the normalized residuals (the differences between the observed count flux and best-fit model count flux, divided by the statistical 1σ uncertainties) are shown below. For the isothermal model, a good fit could not be achieved, especially over the 1.5–20 keV SXR energy range. An additional “cool” thermal component ($T \approx 3$ MK) is required to explain the observed spectrum, as shown in the “two-temperature” model fit. Therefore, in this analysis, the “cool” thermal emission component was always included in the fitting model during the time range of 05:06:14–05:29:24 UT, when spectral analysis is conducted using both MinXSS and RHESSI.

Figure 11 shows the “two-temperature” and “three-temperature” thermal emission models with nonthermal power-law model fits to the observed MinXSS and RHESSI count flux spectra for the 2016-07-23 05:15:04–05:15:14 UT period, near the peak of the flare (time interval E in Figure 6). During the flare peak, the “cool” and “hot” thermal components are not sufficient to explain the observed spectrum, particularly from 10 to 30 keV, and an additional “superhot” thermal component ($T \approx 30$ MK) is required to improve the fit, as seen in both the overall reduced χ^2 statistic and the behavior of the normalized residuals. Therefore, in this analysis, the three-temperature thermal model is used for times after 05:11:14 UT.

¹⁰ <https://lasp.colorado.edu/home/minxss/data/level-0d>

C 2016-07-23 05:10:54 - 05:11:04UT (648 s - 658 s)

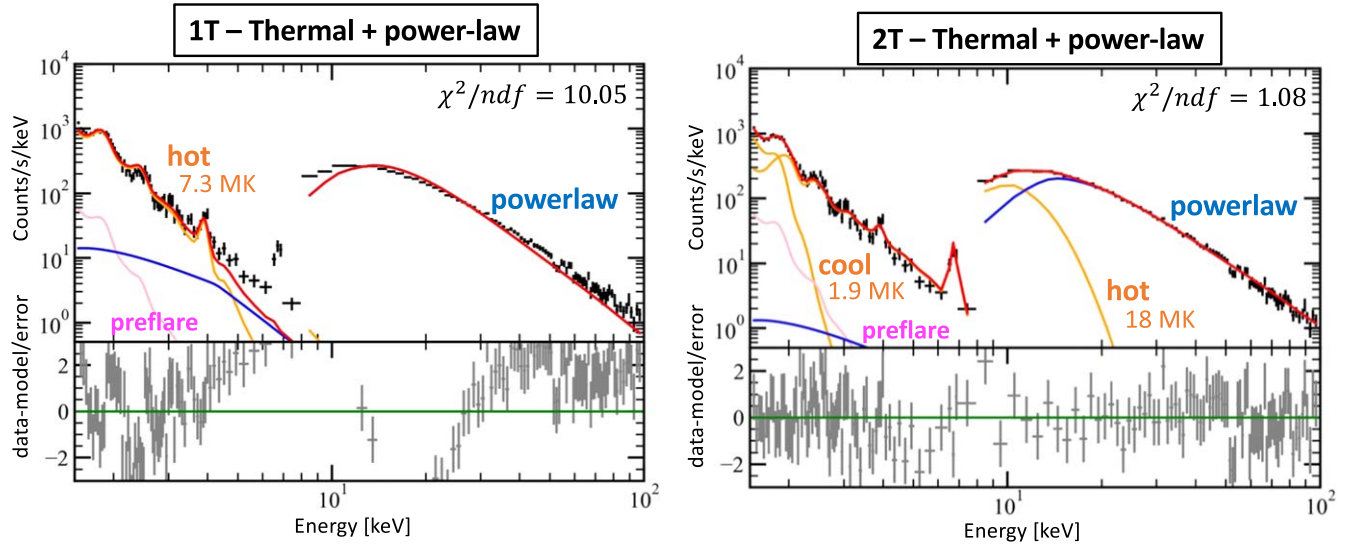


Figure 10. MinXSS and RHESSI count flux spectra and two model fits for the 2016-07-23 05:10:54–05:11:04 UT period (time interval C in Figure 6). Left: isothermal component with nonthermal power-law component. Right: two-temperature thermal components with nonthermal power-law component. Both models are fit over the entire 1.5–100 keV range.

E 2016-07-23 05:15:04 - 05:15:14UT (898 s - 908 s)

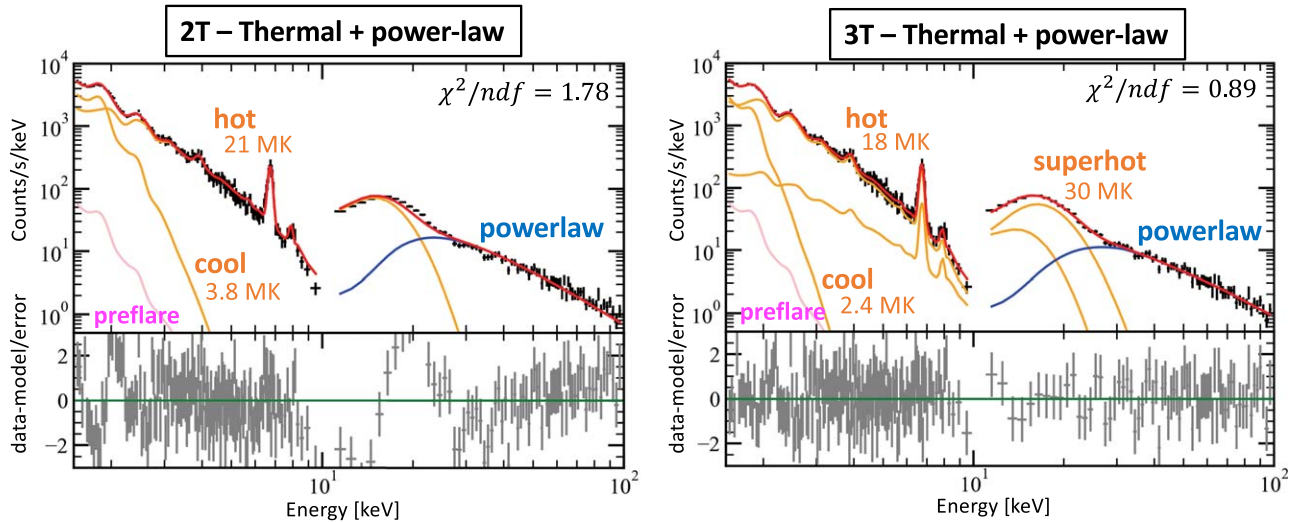


Figure 11. MinXSS and RHESSI count flux spectra and two model fits for the 2016-07-23 05:15:04–05:15:14 UT period (time interval E in Figure 6). Left: two-temperature thermal components with nonthermal power-law component. Right: three-temperature thermal emission with nonthermal power-law model. Both models are fit over the entire 1.5–100 keV range.

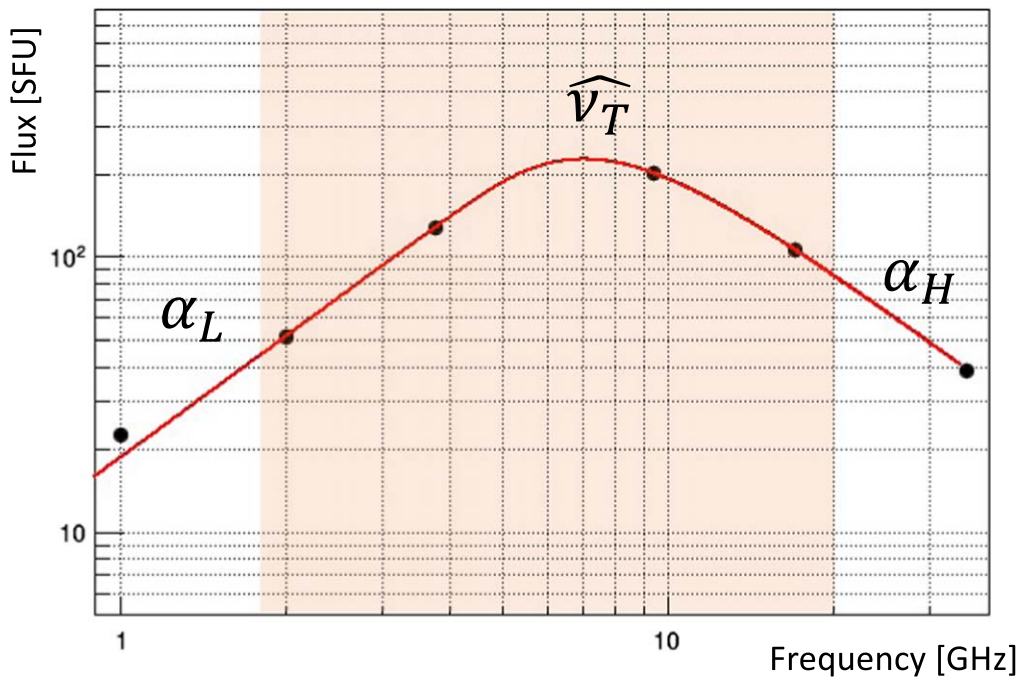


Figure 12. Microwave spectrum taken with NoRP during the 2016 July 23 M7.6 solar flare at 05:12:19–05:12:39 UT. The microwave spectra are integrated over 20 s to improve statistics and are fit using the model described by Equation (C1) over the 2–17 GHz range.

Appendix C Microwave Spectral Fitting

In this study, we fit the NoRP spectra at frequencies of 2, 3.75, 9.4, and 17 GHz, with integration times of 20 s, using a generic model function (Stähli et al. 1989; Silva et al. 2000):

$$F_{\nu} = N \left(\frac{\nu}{\widehat{\nu}_T} \right)^{\alpha_L} \left[1 - \exp \left[- \left(\frac{\nu}{\widehat{\nu}_T} \right)^{\alpha_H - \alpha_L} \right] \right] \\ \approx \begin{cases} N (\nu / \widehat{\nu}_T)^{\alpha_L}, & \text{for } \nu \ll \widehat{\nu}_T \\ N (\nu / \widehat{\nu}_T)^{\alpha_H} & \text{for } \nu \gg \widehat{\nu}_T \end{cases}, \quad (\text{C1})$$

where ν is the frequency and $\widehat{\nu}_T$ is a turnover frequency, and α_L and α_H are the spectral indices at frequencies lower (optically thick) and higher (optically thin), respectively, than the turnover. Figure 12 shows the fitted spectrum at 05:12:19–05:12:39 UT, as an example.

ORCID iDs

Shunsaku Nagasawa <https://orcid.org/0000-0001-6574-6784>

Tomoko Kawate <https://orcid.org/0000-0002-1021-0322>

Noriyuki Narukage <https://orcid.org/0000-0002-6330-3944>

Tadayuki Takahashi <https://orcid.org/0000-0001-6305-3909>

Amir Caspi <https://orcid.org/0000-0001-8702-8273>

Thomas N. Woods <https://orcid.org/0000-0002-2308-6797>

References

Arnaud, K. 1996, *adass*, 101, 17
 Arnaud, K. A., George, I. M., & Tennant, A. F. 2009, The OGIP Spectral File Format, Technical Report, OGIP/92-007
 Athiray, P. S., Winebarger, A. R., Barnes, W. T., et al. 2019, *ApJ*, 884, 24
 Bastian, T. S., Benz, A. O., & Gary, D. E. 1998, *ARA&A*, 36, 131
 Benz, A. 1977, *ApJ*, 211, 270

Benz, A. O. 2017, *LRSP*, 14, 1
 Boerner, P. F., Testa, P., Warren, H., Weber, M. A., & Schrijver, C. J. 2014, *SoPh*, 289, 2377
 Buitrago-Casas, J. C., Vievering, J., Musset, S., et al. 2021, *Proc. SPIE*, 11821, 118210
 Caspi, A., & Lin, R. 2010, *ApJL*, 725, L161
 Caspi, A., McTiernan, J. M., & Warren, H. P. 2014, *ApJL*, 788, L31
 Caspi, A., Shih, A. Y., McTiernan, J. M., & Krucker, S. 2015, *ApJL*, 811, L1
 Caspi, A., Shih, A. Y., Panchapakesan, S., et al. 2021, AAS Meeting, 53, 216
 Cheung, M., Rempel, M., Chintzoglou, G., et al. 2019, *NatAs*, 3, 160
 Dennis, B. R., Phillips, K. J., Schwartz, R. A., et al. 2015, *ApJ*, 803, 67
 Dulk, G. A. 1985, *ARA&A*, 23, 169
 Foster, A., Ji, L., Smith, R., & Brickhouse, N. 2012, *ApJ*, 756, 128
 Garcia, H. A. 1994, *SoPh*, 154, 275
 George, I. M., Arnaud, K. A., Pence, B., & Ruamsuwan, L. 2007, OGIP Calibration Memo CAL/GEN/92-002
 Glesener, L., Buitrago-Casas, J. C., Musset, S., et al. 2020, *AGUFM*, 2020, SH048
 Hannah, I. G., & Kontar, E. P. 2012, *A&A*, 539, A146
 Hesse, M., & Cassak, P. 2020, *JGRA*, 125, e2018JA025935
 Holman, G. D., Aschwanden, M. J., Aurass, H., et al. 2011, *SSRv*, 159, 107
 Hurford, G., Schmahl, E., Schwartz, R., et al. 2002, *SoPh*, 210, 61
 Inglis, A. R., & Christe, S. 2014, *ApJ*, 789, 116
 Kobayashi, K., Winebarger, A. R., Savage, S., et al. 2018, *Proc. SPIE*, 10699, 1069927
 Kosugi, T., Dennis, B. R., & Kai, K. 1988, *ApJ*, 324, 1118
 Krucker, S., Christe, S., Glesener, L., et al. 2009, *Proc. SPIE*, 7437, 743705
 Laming, J. M. 2021, *ApJ*, 909, 17
 Lemen, J. R., Title, A. M., Akin, D. J., et al. 2012, *SoPh*, 275, 17
 Lin, R. P., Dennis, B. R., Hurford, G. J., et al. 2002, *SoPh*, 210, 3
 Machol, J., & Viereck, R. 2016, GOES X-ray Sensor (XRS) Measurements, https://ngdc.noaa.gov/stp/satellite/goes/doc/GOES_XRS_readme.pdf
 Mason, J. P., Woods, T. N., Caspi, A., et al. 2016, *JSpRo*, 53, 328
 Milligan, R. O., & Dennis, B. R. 2009, *ApJ*, 699, 968
 Moore, C. S. 2017, PhD Thesis, University of Colorado, Boulder
 Moore, C. S., Caspi, A., Woods, T. N., et al. 2018, *SoPh*, 293, 1
 Nakajima, H., Sekiguchi, H., Sawa, M., Kai, K., & Kawashima, S. 1985, *PASJ*, 37, 163
 Nakajima, H. A., Nishio, M., Enome, S., et al. 1994, *Proc. IEEE*, 82, 705
 Narukage, N. 2019, *AGUFM*, 2019, SH31C
 Schmelz, J., Reames, D., Von Steiger, R., & Basu, S. 2012, *ApJ*, 755, 33
 Shibata, K. 1996, *AdSpR*, 17, 9
 Shibata, K., & Magara, T. 2011, *LRSP*, 8, 6
 Silva, A. V., Wang, H., & Gary, D. E. 2000, *ApJ*, 545, 1116

Smith, D. M., Lin, R. P., Turin, P., et al. 2002, [SoPh](#), **210**, 33
Stähli, M., Gary, D., & Hurford, G. 1989, [SoPh](#), **120**, 351
Warren, H. P. 2014, [ApJL](#), **786**, L2
Warren, H. P., Mariska, J. T., & Doschek, G. A. 2013, [ApJ](#), **770**, 116
White, S. M., Thomas, R. J., & Schwartz, R. A. 2005, [SoPh](#), **227**, 231

Winebarger, A. R., Warren, H. P., Schmelz, J. T., et al. 2012, [ApJL](#), **746**, L17
Woods, T. N., Caspi, A., Chamberlin, P. C., et al. 2017, [ApJ](#), **835**, 122
Woods, T. N., Eparvier, F. G., Hock, R., et al. 2012, [SoPh](#), **275**, 115
Yokoyama, T., & Shibata, K. 1998, [ApJL](#), **494**, L113